# Dual-Level Control Architectures for Over-Actuated Autonomous Vehicle's Stability, Path-Tracking, and Energy Economy

Fadel Tarhini, Reine Talj, Moustapha Doumiati

# Dual-Level Control Architectures for Over-Actuated Autonomous Vehicle's Stability, Path-Tracking, and Energy Economy

Fadel Tarhini, Reine Talj, and Moustapha Doumiati

***Abstract*—Autonomous vehicles equipped with four independent in-wheel motors bestow salutary design flexibility and render the system over-actuated. The strategy percolated for torque allocation dictates the system's performance and marks its energy consumption. In this paper, two complete novel control architectures are developed and contrasted from the viewpoint of vehicle performance and energy consumption. A cascaded control strategy is employed by incorporating two distinct control levels. The high level is differentiated by a centralized approach based on the optimal $\mathcal{H}_\infty$ control in the framework of the Linear Parameter Varying (LPV) systems, and a decentralized approach based on problem decoupling where a solution is proposed using the Super-Twisting Sliding Mode (STSM) control. Both approaches are supervised by a decision layer to promote the stability objective in critical driving situations. At the low level, stability control based on Direct Yaw Control (DYC) along with speed control are both achieved using an original torque allocation strategy. A comprehensive set of four multi-objective strategies has been devised, centered around a proposed torque allocation configuration. These strategies encompass dynamic online optimization, expertly solved using the highly efficient Sequential Quadratic Programming (SQP) method, as well as a unique offline optimization based on a data-driven implemented algorithm. The proposed architectures are tested and validated in a joint simulation between Simulink/MatLab and SCANeR™ Studio vehicle dynamics simulator. The simulation findings demonstrate substantial improvements in stability, comfort, and energy efficiency at both the high and low levels of the autonomous in-wheel-driven electric vehicle.**

***Index Terms*—Autonomous Vehicle, In-wheel motors, Super-Twisting Sliding Mode (STSM) Control, LPV/$\mathcal{H}_\infty$ Control, Torque Allocation, Online and Offline Optimization.**

## I. Introduction

Transportation electrification is influentially mitigating environmental pollution incurred by the massive combustion of fossil fuels, arbitrated by internal combustion engines. Electric vehicles (EVs) have devoted considerable attention consequent to their zero emissions, high efficiency, and superior driving performances [1]. Controlling EVs to achieve certain objectives requires advanced control algorithms, sophisticated sensors and actuators, and integration with multiple systems. These objectives can solicit the overall motion of the vehicle as in path-tracking, or be confined to the chassis dynamics such as enhancing stability and maneuverability [2].

Fadel Tarhini and Reine Talj are with Université de Technologie de Compiègne, CNRS, Heudiasyc UMR 7253, Compiègne, France (email: fadeltarhini@hotmail.com, reine.talj@hds.utc.fr).

Moustapha Doumiati is with ESEO-IREENA Lab UR 4642, Angers, France (email: moustapha.doumiati@eseo.fr).

### A. Related Works

The segregation of vehicle control into hierarchical layers enables modular development, as each layer can be designed and optimized independently. The hierarchical control architecture comprises two levels: the high level which generates control inputs aligned with desired objectives, and the low level which coordinates actuators to execute those inputs. The actuators coordinate based on advanced assistance systems such as Active Front Steering (AFS) and Direct Yaw Control (DYC). $\mathcal{H}_\infty$ control [3] is employed in [4] to enhance vehicle stability, maneuverability, and roll-over avoidance by coordinating AFS and DYC. [5] presented a non-linear integrated control strategy based on Model Predictive Control (MPC) to maintain vehicle stability using AFS and differential braking. [2] developed centralized and decentralized architectures based on $LPV/\mathcal{H}_\infty$ and Sliding Mode Control targeting only chassis control to maintain stability and handling. However, the comparison was confined only to the performance level.

After the development of increasingly sophisticated control-aided systems, research studies are moving towards the Autonomous Vehicle (AV) to improve road safety. Designing robust control systems that ensure precise and safe AV motion under varying conditions and handling emergency scenarios requires complex control algorithms. [6] presented a safety and comfort-guaranteed automatic following of an autonomous vehicle under several road geometry constraints. A robust adaptive inverse controller is employed in [7] to offset the dynamics of the steering system's backlash. MPC has recently gained significant popularity and has been widely used in AV control. [8] considered path preview to develop an efficient MPC for high-speed lateral motion control. Other studies employed MPC to coordinate path-tracking and DYC [9], [10]. Despite being a valuable control strategy for AVs, MPC relies on an accurate mathematical model and reliable sensor measurements to make predictions and control decisions, during which it typically assumes that the model and the environment remain constant. This can consequently deprive the indispensable aspect of robustness demanded by AVs.

In-wheel vehicles are merging to streamline electric vehicle design and optimize efficiency. The integration of the in-wheel motors on electric vehicles boosts design flexibility, as the system resolves into an over-actuated system that enables independent control of each actuator, for both traction and braking purposes [11], [12]. Hence, the design of advanced controllers to enhance vehicle performance while reducing

consumed energy is conceivable by exploiting the features of such systems. For instance, [13] proposed a multi-layer control method based on robust sliding mode predictive control for in-wheel vehicles to improve maneuverability and lateral stability. Adaptive control schemes were developed in [14], [15] that specifically address chassis control, however, these studies lacked the autonomous aspect that could be integrated into in-wheel vehicles. The MPC-based path-following is heavily investigated for autonomous in-wheel vehicles as in [16] with adaptive adjoining strategy in [17]. While MPC is an optimal control strategy that could be implemented to generate energy-efficient control inputs, it has a computational burden. In particular, when employing a torque allocation strategy for in-wheel motors, which involves solving online optimization problems, real-time execution of MPC may be difficult to achieve. Hence, integrating energy efficiency with computationally efficient robust control methods such as Super-Twisting Sliding Mode (STSM) and $\mathcal{H}_\infty$ control has the potential to bring about a significant impact.

Torque allocation is an effective and widely applied method for controlling in-wheel electric vehicles. It is performed through the distribution of the torques at the wheels by solving constrained control allocation problems that minimize various cost functions [18]–[23]. It is a concise and modular approach to optimize dynamic trade-offs between vehicle performance and energy efficiency. [24] proposed an energy-efficient and real-time implementable torque allocation strategy based on minimizing power losses using offline optimization. [25] presented an energy optimal path-tracking control of an AV considering maximizing battery State Of Charge. However, the employed pattern search optimization method is relatively slow to converge and is sensitive to initial guesses. A hybrid MPC is implemented by [26] to minimize the drive-train power loss while ensuring vehicle stability, yet with a high computational burden. Particle Swarm Optimization (PSO) is employed in [27] to solve a real-time optimal distribution strategy aimed at maximizing the utilization of motors within high-efficiency zones. However, the method suffers premature convergence and exhibits sensitivity to parameter settings. [28] presented an allocation strategy based on dynamic load distribution, yet solely focusing on the redistribution between the front and rear sides of the vehicle without addressing the left/right sides.

### B. Motivations and Contributions

The literature on autonomous vehicle control encompasses diverse perspectives and research directions. Some studies have primarily focused on developing precise path-tracking control, while others have extended their investigations to incorporate stability control, independently of the energy aspects. On the other hand, specific research has centered on in-wheel vehicles, examining the implementation of torque allocation strategies to optimize performance and energy consumption. In this study, a unique approach is taken by combining these distinct elements into a cohesive framework. By integrating stability control over path-tracking with a torque allocation strategy, the aim is to develop a comprehensive methodology that enhances the overall performance

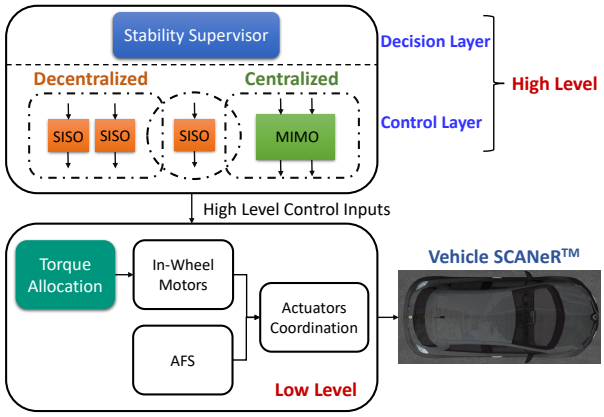


Fig. 1: Proposed Hierarchical Architecture

of the AV. The hierarchical architecture can subsequently be assessed globally on performance and energy economy levels. Therefore, two control architectures are developed based on decentralized STSM and centralized $LPV/\mathcal{H}_\infty$ control at the high level, and four optimal multi-objective-based strategies are established for torque allocation at the low level. The motivation behind these control approaches lies in their robustness. The decentralized STSM is nonlinear, simple to implement, and locally stable while $LPV/\mathcal{H}_\infty$ is linear, complex, and globally stable. The paper will show that the energy economy is achieved not solely at the low level, yet further at the high level.

The contributions of the paper are stated as:

- Development and validation of two novel control layer architectures based on decentralized STSM and centralized $LPV/\mathcal{H}_\infty$ control approaches for path-tracking (lateral control) and speed (longitudinal) control and stability objective promotion based on a decision layer.
- Establishment of an original torque allocation configuration, followed by developing four multi-objective-based strategies for torque allocation including online and offline optimization, and demonstrating that balanced load distribution is an energy quasi-optimal strategy.
- Validation on SCANeR$^{TM}$ Studio simulator to elucidate the merits of using the proposed architectures in the viewpoint of global vehicle performance and overall energy consumption at the high and low levels.

The paper is structured as follows: Section II introduces the global hierarchical control architecture which is divided into high and low levels. Section III illustrates the decentralized STSM and the centralized $LPV/\mathcal{H}_\infty$ high-level architectures. An energy consumption model is developed in Section IV based on a constructed efficiency MAP. Section V demonstrates a novel configuration for torque allocation and develops four multi-objective allocation strategies. System validation is presented in Section VI by exposing simulation-based results. Finally, Section VII presents a conclusion and work perspectives.

## II. Hierarchical Control Architecture

The proposed control architecture is divided into three hierarchical layers that can be congregated into high and low

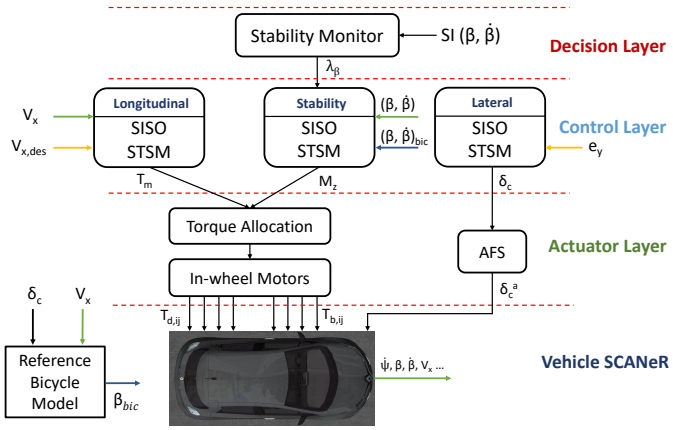


Fig. 2: Proposed Decentralized Architecture

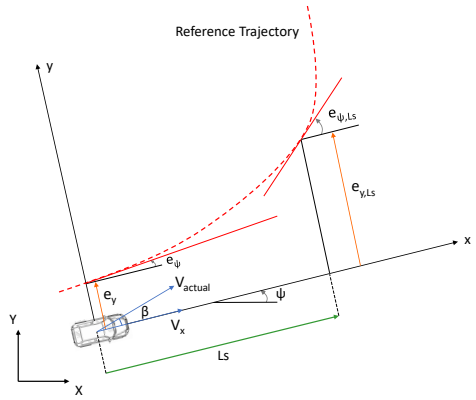


Fig. 3: Lateral Error at a Look-Ahead Distance

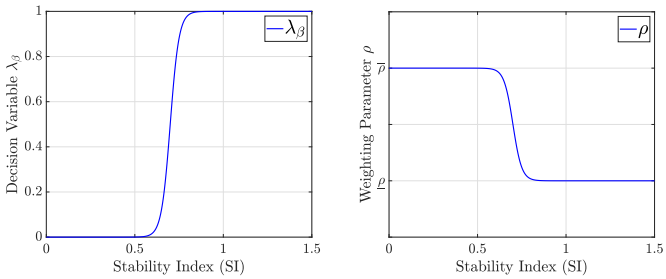


Fig. 4: Decision Parameter $\lambda_\beta$ and Weighting Parameter $\rho$

levels (Fig 1). At the high level, control inputs are generated corresponding to a set of desired objectives to ensure the required performance by the autonomous vehicle. The generation of the control inputs is proceeded in the control layer based on a control technique in the framework of a centralized or decentralized approach. Each control variable reflecting a desired objective is controlled independently using a Single-Input-Single-Output (SISO) controller in the decentralized approach, whereas the centralized approach adopts a unique Multi-Input-Multi-Output (MIMO) controller to generate all the control inputs of interest [29]. Based on a stability index, a decision layer is developed for each approach to coordinate the stability control promotion/attenuation with the remaining objectives –lateral and longitudinal control–, forming a two-layered high-level control. For the rest of the paper, we will refer to the architecture using the centralized approach as the centralized architecture; similarly for the decentralized one. At the low level, the generated control inputs are realized by physical actuators. The actuators designated in this study are the four in-wheel electric motors and the small electric motor of the Active Front Steering (AFS). Lateral control (path-tracking) is achieved by controlling the steering angle using AFS. While longitudinal control (speed control) and stability control (side-slip angle control) are attained by generating a total torque and a yaw moment respectively on the chassis level, then by applying a torque difference among the in-wheel motors using a torque allocation unit. For validation, the fully dynamic "Callas" vehicle of the professional SCANeR$^{TM}$ Studio simulator [30] is controlled to be autonomous. Further, for stability purposes, its side-slip angle is controlled to converge to a linear one given by the reference bicycle model (1), where $\dot{\psi}_{bic}$ and $\beta_{bic}$ are the yaw rate and the side-slip angle of the bicycle model respectively. $\delta_c$ and $M_z$ are the control inputs corresponding respectively to the steering angle and the yaw moment. The rest of the parameters are defined in the Appendix.

$$\begin{pmatrix} \ddot{\psi}_{bic} \\ \dot{\beta}_{bic} \end{pmatrix} = \begin{bmatrix} a_{11} & a_{12} \\ a_{21} & a_{22} \end{bmatrix} \begin{pmatrix} \dot{\psi}_{bic} \\ \beta_{bic} \end{pmatrix} + \begin{bmatrix} b_{11} & b_{12} \\ b_{21} & b_{22} \end{bmatrix} \begin{bmatrix} \delta_c \\ M_z \end{bmatrix} \quad (1)$$

Further, a map-matching module is used for vehicle localization in a global system defined in the corresponding map. An energy consumption model along with an energy-saving criterion are developed which will be illustrated in Section IV.

## III. High Level Control

The high-level control consists of the decision and control layers of the proposed hierarchical control architecture. Two distinct high-level architectures are developed based on centralized and decentralized approaches.

### A. Decentralized STSM Control

#### 1) Super-Twisting Siding Mode (STSM) Technique

The Super-Twisting algorithm is a second-order sliding mode control. In spite of perturbations, it generates the continuous control function that drives the sliding variable and its derivative to reach a sliding surface during a finite time. The reader can refer to [2] for the control technique elaboration and to [31] for the convergence analysis.

#### 2) Coordination of the Control Objectives

The proposed decentralized architecture is shown in Fig. 2. It consists of three decentralized controllers for the lateral, longitudinal, and stability control respectively.

The autonomous vehicle executes the path-following through lateral control. The latter is the last step of a chain of stages consisting of perception and localization. Presuming that the vehicle has access to the required perceptual and localization data, the trajectory can be modeled by a parametric continuous and differentiable curve connecting a sequence of way-points. The lateral displacement error $e_y$ refers to the distance between the vehicle's center of gravity and the reference lane. However, path-tracking is achieved by minimizing the lateral error between the reference lane and a

target point set at a look-ahead distance $Ls$ [32] in front of the vehicle (see Fig. 3). This distance is denoted by $e_{y,Ls}$ and is necessitated to take into account the delay of the sensors and controllers/actuators. Finally, lateral control is executed by controlling the steering angle $\delta_c$ via the Active Front Steering (AFS) mechanism to minimize $e_{y,Ls}$.

For the on-road vehicle, its longitudinal velocity should vary in real-time to adhere to the rules of the road and achieve a level of comfort for the passengers. Hence, a desired velocity reference profile $V_{x_{des}}$ (2) is constructed by considering a comfort criterion to keep the lateral acceleration under a threshold $a_{y_{max}} = 4\ m/s^2$ [33] while imposing limitations according to the road rules $V_{x_{lim}}$, where $\chi$ denotes the road curvature. Then, longitudinal control is executed by controlling the longitudinal velocity to track the reference profile, by applying a total traction torque $T_m$.

$$V_{x_{des}} = \min\left(\sqrt{\frac{a_{y_{max}}}{\chi}}, V_{x_{lim}}\right) \tag{2}$$

As for the non-deterministic environment, the on-road vehicle may encounter complex situations for instance sudden steering for object avoidance or moving on low-adherence roads. Under these situations, the vehicle will lose stability consequently leading to an accident. Hence, a supervisory strategy is developed based on a decision layer to promote and attenuate stability control based on road situations. The lateral stability index $SI$ (3) as defined in [29] is utilized to monitor the driving situations, and a weighting parameter $\lambda_\beta$ (5b) (Fig. 4) is computed in real-time to promote/attenuate the control of the side-slip angle $\beta$ to track the reference bicycle model.

$$SI = |2.49\dot{\beta} + 9.55\beta| \tag{3}$$

When $SI$ is under a positive threshold $\underline{SI} = 0.6$, the vehicle is in normal driving situations and the stability control is relaxed ($\lambda_\beta = 0$). Whilst, a critical driving situation is monitored when $SI \geq \overline{SI} = 0.8$ and the stability control is promoted accordingly (as $\lambda_\beta$ approaches 1). Stability control is achieved by generating a corrective yaw moment $M_z$ using the Direct Yaw Control (DYC) mechanism.

*3) Control Problem Formulation*

Three decentralized controllers are developed to independently control the lateral, longitudinal, and stability objectives. To this end, let's define the sliding variables as

$$s_y = \dot{e}_{y,Ls} + k_y e_{y,Ls}; \quad \text{with } k_y > 0 \tag{4a}$$

$$s_x = (V_x - V_{x_{des}}) + k_x \int (V_x - V_{x_{des}})\, dt; \quad k_x > 0 \tag{4b}$$

$$s_\beta = \dot{e}_\beta + k_\beta\, e_\beta = (\dot{\beta} - \dot{\beta}_{ref}) + k_\beta\, (\beta - \beta_{ref}); \quad k_\beta > 0 \tag{4c}$$

where $s_y$, $s_x$, and $s_\beta$ have a relative degree equal to 1 w.r.t their corresponding control inputs $\delta_c$, $T_m$, and $M_z$ respectively (refer to [11] for the longitudinal dynamics effect), and

$$\beta_{ref} = \lambda_\beta \beta_{bic} + (1 - \lambda_\beta)\beta \tag{5a}$$

$$\lambda_\beta = \frac{1}{1 + e^{-\frac{8}{\overline{SI} - \underline{SI}}\left(SI - \frac{\overline{SI} + \underline{SI}}{2}\right)}} \tag{5b}$$

where $\beta_{bic}$ is the side-slip angle of the bicycle model.

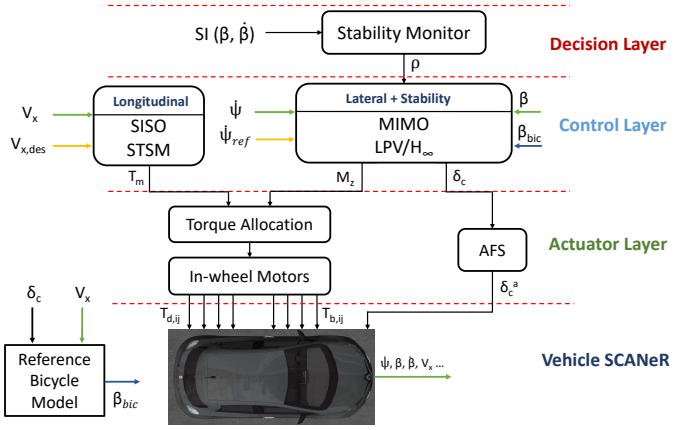


Fig. 5: Proposed Centralized Architecture

Assume that there exist $S_0$, $b_{min}$, $b_{max}$, $C_0$, $U_{max}$ verifying (6) for all x $\in \mathbb{R}^n$ and $|s(x,t)| < S_0$ (see [31]).

$$\begin{cases} |u(t)| \leq U_{max} \\ |\Phi(s,t)| < C_0 \\ 0 < b_{min} \leq |\xi(s,t)| \leq b_{max} \end{cases} \tag{6}$$

Therefore, the control inputs corresponding respectively to lateral, longitudinal, and stability control are given by

$$\delta_c = -\alpha_{\delta_c,1}|s_y|^{\tau_{\delta_c}} sign(s_y) - \alpha_{\delta_c,2}\int_0^t sign(s_y)\, d\tau, \tag{7a}$$

$$T_m = -\alpha_{T_m,1}|s_x|^{\tau_{T_m}} sign(s_x) - \alpha_{T_m,2}\int_0^t sign(s_x)\, d\tau \tag{7b}$$

$$M_z = -\alpha_{M_z,1}|s_\beta|^{\tau_{M_z}} sign(s_\beta) - \alpha_{M_z,2}\int_0^t sign(s_\beta)\, d\tau \tag{7c}$$

where $\alpha_{\delta_c,i}$, $\alpha_{T_m,i}$, and $\alpha_{M_z,i}$ with i = [1,2] are positive constants satisfying the conditions (8), and $\tau_{\delta_c}$, $\tau_{T_m}$, and $\tau_{M_z}$ are constants in the interval ]0,0.5]. An approximation function $\frac{s}{|s|+\epsilon}$ is used to smooth the sign(s) function, where $\epsilon > 0$.

$$\begin{cases} \alpha_1 \geq \sqrt{\frac{4C_0(b_{max}\alpha_2 + C_0)}{b_{min}^2(b_{min}\alpha_2 - C_0)}} \\ \alpha_2 > \frac{C_0}{b_{min}} \end{cases} \tag{8}$$

The STSM control inputs $\delta_c$ (7a), $T_m$ (7b), and $M_z$ (7c) respectively guarantee the convergence of $s_y$, $s_x$, and $s_\beta$ to zero in a finite time. Once reaching the sliding surface, $e_{y,Ls}$, $e_\beta$ and $e_x = V_x - V_{x_{des}}$ converge exponentially to zero with rates $k_y > 0$, $k_\beta > 0$, and $k_x > 0$, respectively.

## B. Centralized LPV/$\mathcal{H}_\infty$ Control

*1) Centralized Architecture*

Similar to the decision layer of the decentralized architecture, the stability supervisor monitors the stability index of the vehicle to generate a weighting parameter $\rho$ (according to Fig. 4). The proposed centralized architecture is given in Fig. 5. The control layer is composed of a centralized MIMO controller that generates the controlled steering angle $\delta_c$ and the yaw moment $M_z$, and a SISO controller for the sake of longitudinal control as in Section III-A. Longitudinal control is secluded from the MIMO controller to avoid the high complexity of the system. Developing a comprehensive LPV model that captures both longitudinal and lateral dynamics

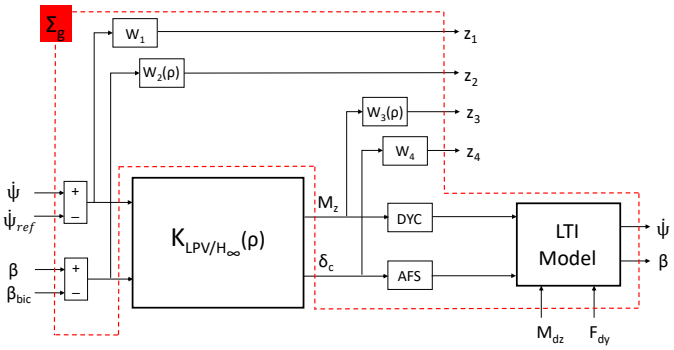


Fig. 6: Centralized Control Layer Architecture

falls outside the scope of the paper. Unlike the decentralized case where the lateral control is achieved by directly regulating the lateral error $e_{y,Ls}$, the path-tracking in the centralized approach is realized by controlling the yaw rate to track a reference $\dot{\psi}_{ref}$ (9). The underlying reason is the form of the plant defined later, which incorporates $\dot{\psi}$ and $\beta$. The reference yaw rate is an image of the lateral error and it is generated in real-time based on the lateral error $e_{y,Ls}$, the look-ahead distance $Ls$, and the vehicle longitudinal velocity $V_x$ (see [34]).

$$\dot{\psi}_{ref} = -\frac{2V_x e_{y,Ls}}{Ls^2} \tag{9}$$

An extension of the bicycle model (1) is performed to include external disturbances $M_{dz}$ and $F_{dy}$ influencing directly the yaw moment and the side-slip angle respectively. This extension permits the synthesizing of a robust controller for disturbance rejection. The extended model is denoted by plant *P* reflecting a Linear-Time-Invariant (LTI) system (10), where $c_1$, $c_2$ are given in the Appendix.

$$\begin{pmatrix} \ddot{\psi} \\ \dot{\beta} \end{pmatrix} = \begin{bmatrix} a_{11} & a_{12} \\ a_{21} & a_{22} \end{bmatrix} \begin{pmatrix} \dot{\psi} \\ \beta \end{pmatrix} + \begin{bmatrix} b_{11} & b_{12} \\ b_{21} & b_{22} \end{bmatrix} \begin{bmatrix} \delta_c \\ M_z \end{bmatrix} + \begin{bmatrix} c_1 & 0 \\ 0 & c_2 \end{bmatrix} \begin{bmatrix} M_{dz} \\ F_{dy} \end{bmatrix} \tag{10}$$

Subject to vehicle autonomy, AFS is consistently active to minimize the yaw rate error, in order to track the trajectory. As for the stability control, DYC is activated to minimize the side-slip angle error (when necessary) based on the weighting parameter $\rho$ (11) given in Fig. 4.

$$\rho = \overline{\rho} - \frac{\overline{\rho} - \underline{\rho}}{1 + e^{-\frac{8}{\overline{SI} - \underline{SI}}(SI - \frac{\overline{SI} + \underline{SI}}{2})}} \tag{11}$$

The yaw moment $M_z$ will be applied using a torque difference generated by torque signals given by the in-wheel motors at the low level.

*2) Control Problem Formulation*

The $\mathcal{H}_\infty$ control synthesis is a disturbance attenuation problem. It consists of finding a stabilizing controller that minimizes the impact of input disturbances $w(t)$ on a weighted controlled output $z(t)$. The plant *P* together with the performance weighting functions $W_i$ form a generalized plant $\Sigma_g$. The formulation of the standard $\mathcal{H}_\infty$ controller structure is given in Fig. 6. The weighting functions $W_1$, $W_2$, $W_3$, and $W_4$ are defined to characterize the performance objectives $z_1$, $z_2$ and the actuator limitations $z_3$, $z_4$. The general forms are inspired from [35], [36]. The novelty here is the constant weighting of $W_1$ and $W_4$ tuned by $\varrho$. In addition to the design of $W_3$ that weights the in-wheel motor torque signal for traction and braking, contrary to prior approaches [3], [35] that solely focused on the braking control signal. $\varrho$ is tuned to amplify the magnitude response of the filter to adjust the path-tracking performance.

- $W_1$ weights the yaw rate error signal ($e_{\dot{\psi}} = \dot{\psi} - \dot{\psi}_{ref}$)

$$W_1 = \varrho \frac{s/M_1 + 2\pi f_1}{s + 2\pi f_1 A_1}, \tag{12}$$

  where $\varrho$ is a positive constant used for weighting, $M_1$ is sufficiently high for a large robustness margin, and $A_1$ is the tolerated tracking error on $e_{\dot{\psi}}$. $W_1$ is a constant weight shaped to permanently reduce $e_{\dot{\psi}}$ in the range of frequencies below the roll-off frequency $f_1$.
- $W_2$ weights the side-slip angle error signal ($\beta - \beta_{bic}$)

$$W_2 = \frac{1}{\rho} \frac{s/M_2 + 2\pi f_2}{s + 2\pi f_2 A_2}, \tag{13}$$

  where $M_2$, $A_2$ and $f_2$ have similar meanings as $M_1$, $A_1$ and $f_1$. The filter is designed with dependency on the weighting parameter $\rho$ (Fig. 4). When $SI \leq \underline{SI}$, $\rho$ is assigned by its maximal value $\overline{\rho}$ and the minimization of the side-slip angle error $e_\beta$ is relaxed. Whilst $\rho$ decreases to reach $\underline{\rho}$ as $SI$ increases above $\overline{SI}$ where the minimization of $e_\beta$ is promoted.
- $W_3$ weights the motor torque signal to generate $M_z$

$$W_3 = \rho \frac{s/(2\pi f_3) + 1}{s/(\alpha 2\pi f_3) + 1} \times 10^{-5}, \tag{14}$$

  where $f_3$ is the motor actuator cut-off frequency and $\alpha$ handles the motor actuator limitations. When $\rho = \underline{\rho}$, the motor control signal is promoted, on the contrary, when $\rho = \overline{\rho}$, the motor control input is penalized.
- $W_4$ weights the steering control signal $\delta_c$

$$W_4 = \frac{1}{\varrho} \frac{s + 2\pi f_4/\nu}{\varepsilon s + 2\pi f_4}, \tag{15}$$

  where $\nu$ imposes limitations on the maximum allowed effort of the actuator, $\varepsilon$ concerns the noise rejection from the control inputs at high frequencies, and $f_4$ as $f_1$.

The generalized plant $\Sigma_g$ is polytopic LPV [37] and can be formulated as

$$\Sigma_g(\rho): \begin{bmatrix} \dot{x} \\ z \\ y \end{bmatrix} = \begin{bmatrix} A(\rho) & B_1(\rho) & B_2 \\ C_1(\rho) & D_{11}(\rho) & D_{12} \\ C_2 & D_{21} & 0 \end{bmatrix} \begin{bmatrix} x \\ w \\ u \end{bmatrix}, \tag{16}$$

where $\rho$ is the weighting parameter, $x$ includes the state variables of the LTI plant *P* and the weighting functions $W_i$, $w = [\dot{\psi}_{ref}, \beta_{bic}, M_{dz}, F_{dy}]^T$ is the exogenous input vector, $u = [\delta_c, M_z]^T$ represents the control inputs, $y = [\dot{\psi}, \beta]^T$ is the measurement vector fed-back to the controller and $z = [z_1, z_2, z_3, z_4]^T$ is the weighted controlled output vector. Note that the estimation of $\beta$ is considered accessible. The requirements of $\mathcal{H}_\infty$ for polytopic systems restrain the matrices $B_2$ and $D_{12}$ from the dependency on $\rho$, hence a filter has been utilized on the control input to relax the mentioned issue [37].

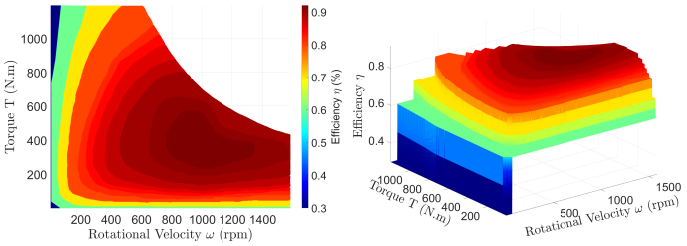


Fig. 7: In-Wheel Motor Efficiency: Motoring

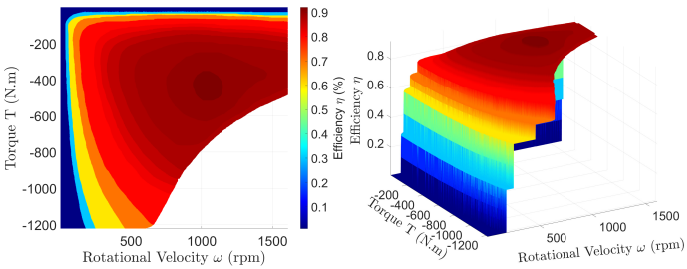


Fig. 8: In-Wheel Motor Efficiency: Regenerative Braking

*3) Problem resolution: LMI based LPV/$\mathcal{H}_\infty$*

The $LPV/\mathcal{H}_\infty$ problem consists in finding the controller $K_{LPV/\mathcal{H}_\infty}(\rho)$, scheduled by the parameter $\rho$, such that:

$$K_{LPV/\mathcal{H}_\infty}(\rho): \begin{bmatrix} \dot{x}_c \\ u \end{bmatrix} = \begin{bmatrix} A_c(\rho) & B_c(\rho) \\ C_c(\rho) & 0 \end{bmatrix} \begin{bmatrix} x_c \\ y \end{bmatrix} \quad (17)$$

which minimizes the $\mathcal{H}_\infty$ norm of the closed-loop $LPV$ system formed by the interconnection of equations (16) and (17). The formulated problem can be solved using several approaches, for instance, polytopic, gridding, or the Linear Fractional Transformation approach [36]. In this paper, a polytopic approach [37] is adopted for controller synthesis. The reader can refer to the author's previous work [35] for the complete synthesis. A non-conservative $LMI$ that expresses the same problem as the Bounded Real Lemma $BRL$ is formulated (see [35]) and solved offline for $\rho \in \Omega = [\underline{\rho}, \overline{\rho}]$. Therefore, in consonance with the polytopic approach, the applied controller $K_{LPV/\mathcal{H}_\infty}(\rho)$, is a convex combination of the controllers synthesized at the vertices of $\Omega$ [37] such as:

$$K_{LPV/\mathcal{H}_\infty}(\rho) = \alpha_1 K_{LPV/\mathcal{H}_\infty}(\underline{\rho}) + \alpha_2 K_{LPV/\mathcal{H}_\infty}(\overline{\rho}), \quad (18)$$

with,

$$\alpha_1 = \frac{\rho - \overline{\rho}}{\overline{\rho} - \underline{\rho}}; \qquad \alpha_2 = \frac{\rho - \underline{\rho}}{\overline{\rho} - \underline{\rho}} \quad (19)$$

## IV. Energy Consumption Model

This section is dedicated to introducing a new criterion for determining the amount of energy savings. The terms introduced in this section will be used later to evaluate the developed architectures.

### A. Power Consumption

The power consumption of the four motors is given by (20) and depends on the efficiency of each motor. As the power loss of the battery is considered negligible, the output power

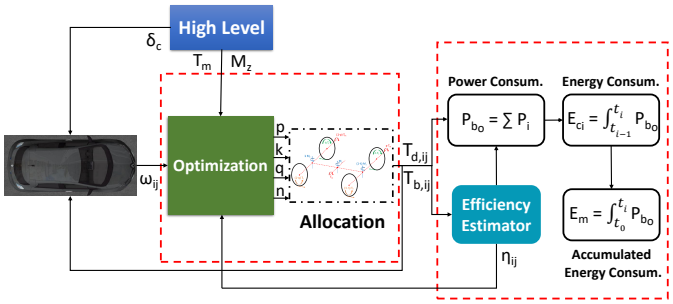


Fig. 9: Low Level Control Architecture

of the battery, $P_{bo}$, equates to the instantaneous total power consumption of the four in-wheel motors.

$$P_{bo} = \sum_{i=1}^{4} P_i = \sum_{i=1}^{4} \frac{T_i \omega_i}{\eta_{k,i}^{sign(T_i)}} \quad (20)$$

where $\eta_k = \eta_d$ corresponding to motoring/driving efficiency if $T_i \geq 0$, whilst $\eta_k = \eta_b$ corresponding to regenerative braking efficiency otherwise. $T_i$ and $\omega_i$ correspond respectively to the motor's total traction/braking torque and its rotational velocity. The total torque acting on each wheel is expressed as $T_i = T_{d,i} - T_{b,i}$, where $T_{d,i}$ and $T_{b,i}$ are respectively the traction and braking torques. The motor efficiency depends on the torque generated by the motor and its angular velocity. The relation $\eta = f(T, \omega)$ is denoted by the motor efficiency MAP. Due to the high order and nonlinearity of the motor system, obtaining an explicit form of efficiency is extremely difficult. Thus, the efficiency estimation is performed using Look-Up Tables (LUTs) visualized in the form of MAPs. The efficiency MAPs for the PD18 DC electric in-wheel motor [38] are constructed for motoring (traction torques) and for regenerative braking (braking torques) in Fig. 7, 8 respectively. $\eta$ is estimated through the LUT based on a linear point-slope interpolation using the binary search method.

### B. Energy Consumption

The process of accumulated energy consumption refers to the entire energy consumed from the initial instant $t_0$ until the current instant $t_i$. Figure 9 reveals the energy consumption model posterior to torque allocation at the low level, where $p, k, q, n$ are allocation parameters which will be introduced later.

The criterion for determining the amount of energy saved as a result of the optimization is to compute the relative change in energy consumption from a vehicle with an optimized torque distribution to a vehicle without. The comparison is performed with a reference vehicle (denoted by "classical vehicle"), which is distinguished by distributing the traction torques uniformly on the four wheels and generating $M_z$ using half-traction / half-braking on the vehicle's opposite sides. Therefore, the criterion is to apply the performance energy index $E_g$ (Fig. 10) on the accumulated energy consumption of the two vehicles, where $E_{m_{OP}}$ and $E_m$ are respectively the energy consumed by the vehicle with optimized torque distribution and the classical vehicle. The energy gain $E_g$ depicts the percentage of energy saved by optimally distributing the torques while minimizing energy consumption. The total

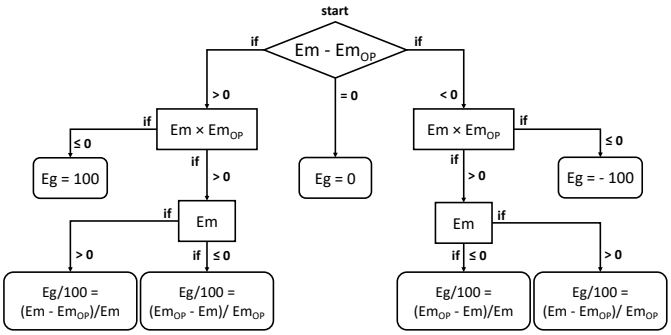


Fig. 10: Proposed Energy Performance Index $E_g$ (%)

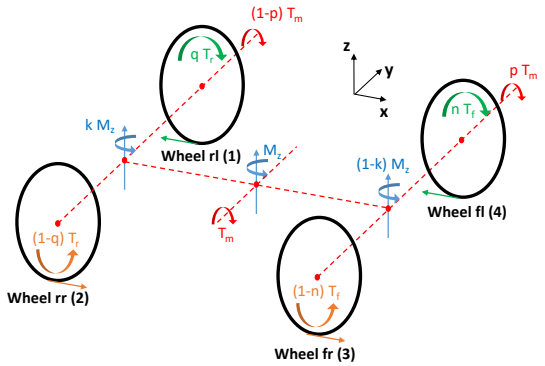


Fig. 11: Proposed Torque Allocation for a ccw $M_z$

energy gain represents the overall saving percentage specified by the final instant $t_{end}$ at the end of the test.

## V. Low Level Control

Following the generation of the control inputs for lateral, longitudinal, and stability control objectives at the high level, $\delta_c$ is realized by AFS at the low level. Whilst, $M_z$ is achieved using the Direct Yaw Control (DYC) by distributing the torques among the motors, along with $T_m$ within a torque allocation unit. First, a novel configuration for torque allocation will be introduced followed by developing the multi-objective-based strategies.

### A. Proposed Allocation Strategy

To reap the benefits of the over-actuation of the system, torques must be dispersed using the maximum possible Degrees Of Freedom (DOF). Indeed, there are four driving and four braking torques that can be realized by the actuators; however, there is a set of constraints to be imposed on the distribution configuration, thereby decreasing the number of DOF possible. To avoid interference with the generation of $M_z$, every wheel on the same axle must receive similar torques, and the sum of the four driving torques must be equal to $T_m$ (21).

$$\begin{aligned} T_m &= T_{d,rl} + T_{d,rr} + T_{d,fr} + T_{d,fl} \\ T_{d,il} &= T_{d,ir} \end{aligned} \tag{21}$$

where $T_{d,ij}$ is the driving torque acting on the wheel $ij$, and $i$, $j$ = [rear (r), front (f)], [right (r), left (l)]. Note that $T_i = T_1, T_2, T_3, T_4$ (20) respectively corresponds to $T_{rl}$, $T_{rr}$, $T_{fr}$, $T_{fl}$. Imposing these constraints on $T_{d,ij}$, the driving torque allocation (22) resulted. Therefore, the total motor torque $T_m$ is weighted by a variable $p$ on the front axle, and $(1-p)$ on the rear one.

$$\begin{cases} T_{d,rl} = T_{d,rr} = \frac{T_m}{2}(1-p) \\ T_{d,fl} = T_{d,fr} = \frac{T_m}{2}(p) \end{cases} \quad \text{where } 0 \le p \le 1 \tag{22}$$

The constraints (21) are imposed into the variable $p$ and modulated as $p$ between 0 and 1. To enable the development of $M_z$ utilizing the four wheels, its generation is split between the front and rear sides of the vehicle, resulting in two centers of rotation, one on each of the front and rear axles. This is achieved by weighting $M_z$ by a parameter $k$ on the rear axle and $(1-k)$ on the front axle. The moment is converted into wheel torque by multiplying it by the ratio of the wheel effective radius $r$ to the half-track $t_r$. Therefore, $M_z$ is formed by generating two total torques $T_r$ and $T_f$ on the rear and front axles, respectively.

$$\begin{cases} T_r = \frac{-r}{t_r}\, kM_z \\ T_f = \frac{-r}{t_r}\,(1-k)M_z \end{cases} \quad \text{where } 0 \le k \le 1 \tag{23}$$

Assuming small $\delta_c$ and considering a counter-clockwise (ccw) $M_z$ generation,

$$\frac{M_z}{t_r} = -F_{x,rl} + F_{x,rr} - F_{x,fl} + F_{x,fl}, \tag{24}$$

where $F_{x,ij}$ is the wheel $ij$ longitudinal force. $T_r$ and $T_f$ are distributed between the left and right sides by a combination of deceleration and acceleration on the vehicle's both sides according to the direction of $M_z$. In order to avoid excessive acceleration/braking, $T_r$ and $T_f$ are distributed by braking on one side (two wheels on the same side) and acceleration on the other. These constraints, along with (24) are imposed in the parameters $k, q, n$. The distribution between both sides of the vehicle is done by weighting the total rear torque $T_r$ by $q$ for braking and $(1-q)$ for accelerating. Similarly, $T_f$ is weighted by $n$ for braking and $(1-n)$ for accelerating.

$$\begin{cases} T_{b,rr} = qT_r \\ T_{b,fr} = nT_f \\ T_{d,rl} = (1-q)T_r \\ T_{d,fl} = (1-n)T_f \end{cases} \tag{25}$$

$$\begin{cases} T_{b,rl} = qT_r \\ T_{b,fl} = nT_f \\ T_{d,rr} = (1-q)T_r \\ T_{d,fr} = (1-n)T_f \end{cases} \tag{26}$$

The allocation depends on the direction of $M_z$. Torques are distributed as in (25) if the required $M_z$ is in the clockwise direction, and according to (26) otherwise, where $q, n \in [0,\ 1]$ and $T_{b,ij}$ represent the wheel $ij$ braking torque.

$$\begin{cases} T_{b,rl} = q\frac{-r}{t_r}\, kM_z \\ T_{b,fl} = n\frac{-r}{t_r}\,(1-k)M_z \\ T_{b,rr} = T_{b,fr} = 0 \\ T_{d,rl} = (1-p)\frac{T_m}{2} \\ T_{d,rr} = (1-p)\frac{T_m}{2} + (1-q)\frac{-r}{t_r}\, kM_z \\ T_{d,fl} = p\frac{T_m}{2} \\ T_{d,fr} = p\frac{T_m}{2} + (1-n)\frac{-r}{t_r}\,(1-k)M_z \end{cases} \tag{27}$$

Combining (22, 23, 25, 26) leads to the allocation (27) for ccw $M_z$ and (28) otherwise, where $p, k, q, n \in [0,\ 1]$. Therefore,

the traction and braking torques are distributed according to the illustrated configuration Fig. 11, depending on the four parameters $p, k, q, n$.

$$\begin{cases} T_{b,rr} = q\frac{r}{t_r}\ kM_z \\ T_{b,fr} = n\frac{r}{t_r}\ (1-k)M_z \\ T_{b,rl} = T_{b,fl} = 0 \\ T_{d,rr} = (1-p)\frac{T_m}{2} \\ T_{d,rl} = (1-p)\frac{T_m}{2} + (1-q)\frac{r}{t_r}\ kM_z \\ T_{d,fr} = p\frac{T_m}{2} \\ T_{d,fl} = p\frac{T_m}{2} + (1-n)\frac{r}{t_r}\ (1-k)M_z \end{cases} \tag{28}$$

Imposing the constraints on the low level to be directly carried by the four parameters reduces the computational time of the allocation, simplifies the problem formulation, and clarifies the feasibility of the optimization problem defined later.

### B. Physical Actuators

To approach reality, the dynamic response of the actuators to control input signals should be considered. For this purpose, simple models that represent the physical actuators have been studied. The AFS actuator is modeled as a Low-Pass Filter (LPF) with a cut-off frequency $f_\delta$ (29), where it saturates at $\delta^a_{c,max}$. Hence it is bounded in the range $[-\delta^a_{c,max}, \delta^a_{c,max}]$.

$$\dot{\delta}^a_c = 2\pi f_\delta(\delta_c - \delta^a_c) \tag{29}$$

A simplified first-order electric model is applied to relate the torque command given at the low level at each wheel $T_{ij}$, and the effective motor torque generated by the electric motor $T^*_{ij}$.

$$T^*_{ij} = \frac{T_{ij}}{1 + \frac{L_m}{R_m}s};\ \text{with}\ \ f_m = \frac{R_m}{2\pi L_m} \tag{30}$$

where $L_m$ and $R_m$ are respectively the motor's internal inductance and resistance, and $f_m$ is the cut-off frequency of the LPF. $T_{ij}$ is saturated at $T^*_{max}$, hence it is bounded between $[-T^*_{max}, T^*_{max}]$.

### C. Energy Economic Optimization Approach

The high-level constraint that torque allocation is dependent on control inputs generated at the current time instant limits power consumption to be instantaneous and drives its realization to be unanticipated.

$$E_{tot} = \int P_{bo}\, dt = \int \sum_{i=1}^{4} \frac{T_i\omega_i}{\eta_i^{sign(Ti)}}\, dt \tag{31}$$

The objective function desired to be minimized is the total energy given in (31). Since the power consumption can't be predicted, the integration of the battery power couldn't be formalized. Hence, instead of minimizing the energy consumption over a time zone, it is sufficient to minimize the instantaneous power consumption. Therefore, the minimization of $E_{tot}$ is equivalent to minimizing $P_{bo}$ per sample time (32). This concept is held when the power loss of the battery is neglected [39].

$$min \int P_{bo}\, dt \Leftrightarrow min\ P_{bo} \tag{32}$$

Hence, the problem is transformed into an instantaneous optimization problem of determining $T$ satisfying (33), i.e. the optimization problem turns into finding the four parameters $p, k, q, n \in [0, 1]$ at each instant, that minimize a cost function which resembles the power consumption.

$$\min_{T(p,k,q,n)} \quad \sum_{i=1}^{4} \frac{T_i\omega_i}{\eta_i^{sign(T_i)}} \tag{33}$$

It is also important to stress that each set of the parameters $p, k, q, n \in [0, 1]$ consistently guarantees the realization of the high-level control inputs $M_z$ and $T_m$.

### D. Multi-Objective-Based Allocation Strategies

The reduction in the vehicle's energy consumption entails finding the optimal parameters' values that minimize a cost function reflecting a set of desired objectives. Any set of values for $p, k, q, n$ that satisfies their constraints $[0, 1]$ represents a feasible solution for the optimization problem (33). Four strategies are developed considering distinct multi-objectives. Some strategies are energy quasi-optimal, yet simultaneously reflecting that a torque allocation based on balanced (either static or dynamic) load transfer is effective in preserving the energy. The initial pair of strategies is founded upon balanced load distribution, and they are categorized as multi-objective approaches, as they address load transfer to ensure the simultaneous preservation of stability and passenger comfort.

#### 1) Constant Parameters: Static Load Distribution

The idiom of "constant parameters" comes from setting the allocation parameters $p, k, q, n$ constants as (34) based on a static load distribution, where $l_r$, $l_f$ are the distances from the center of gravity to the rear and front axles respectively, and $t_r$, $t_f$ are the half rear and half front tracks respectively.

$$p = \frac{l_r}{l_f + l_r}; \quad k = \frac{l_f}{l_f + l_r}; \tag{34a}$$

$$q = \frac{t_r}{t_f + t_r}; \quad n = \frac{t_f}{t_f + t_r}, \tag{34b}$$

The tested vehicle has similar tracks ($t_r = t_f$) which in terms effectuate assigning $q, n$ as $1/2$, forcing the sum of the longitudinal forces acting on the wheels to become 0; consequently minimizing the system interference with the longitudinal dynamics. This attainment stands as an additional realized objective of this strategy.

#### 2) Dynamic Load Distribution

The aim of this strategy is to allocate torques by considering the dynamic load distribution between both the front and rear and the right and left sides of the vehicle. The Tire Working-Load Usage (TWU) (35) represents the edges of the friction circle [40]. The basic idea behind the friction circle is to impose a limit on the longitudinal forces $F_{x,i}$ acting on the wheels due to the existence of the lateral forces $F_{y,i}$. As TWU is smaller i.e. the friction circle of the wheel is larger, as the wheel has more adhesion (of coefficient $\mu$) to the ground, thus has the ability to have larger torques.

$$TWU = \sum_{i=1}^{4} \frac{F^2_{x,i} + F^2_{y,i}}{(\mu F_{z,i})^2} \tag{35}$$

Let's define two load distribution ratios $\kappa_1$ and $\kappa_2$ as

$$\kappa_1 = \frac{F_{z,fi}}{F_{z,ri}} = \frac{F_{z,fr} + F_{z,fl}}{F_{z,rr} + F_{z,rl}} \tag{36a}$$

$$\kappa_2 = \frac{F_{z,ir}}{F_{z,il}} = \frac{F_{z,fr} + F_{z,rr}}{F_{z,fl} + F_{z,rl}} \tag{36b}$$

The strategy is to make the ratio of the longitudinal forces proportional to the loads $F_{z,i}$, between the rear/front sides and left/right sides of the vehicle.
Hence, $\kappa_1$ is reformulated as

$$\kappa_1 = \frac{F_{x,f}}{F_{x,r}} = \frac{pT_m/r}{(1-p)T_m/r} \tag{37}$$

And $\kappa_2$ is reformulated depending on the direction of $M_z$

$$\upsilon = \frac{q(r/t_r)kM_z + q(r/t_f)(1-k)M_z}{(1-q)(r/t_r)kM_z + (1-q)(r/t_f)(1-k)M_z} \tag{38a}$$

$$\kappa_2 = \begin{cases} \upsilon & \text{if } M_z \text{ is counter-clockwise} \\ 1/\upsilon & \text{if } M_z \text{ is clockwise} \end{cases} \tag{38b}$$

where wheels having larger friction circles receive traction torques, whereas those with lower friction circles receive braking torques.
Therefore, the allocation parameters are formulated as

$$\begin{aligned} p &= \frac{F_{z,f}}{F_{z,f} + F_{z,r}} = \frac{\kappa_1}{1+\kappa_1} \\ k &= 1 - p = \frac{1}{1+\kappa_1} \\ q = n &= \begin{cases} \frac{\kappa_2}{1+\kappa_2} & \text{if } M_z \text{ is counter-clockwise} \\ \frac{1}{1+\kappa_2} & \text{if } M_z \text{ is clockwise} \end{cases} \end{aligned} \tag{39}$$

where $\kappa_1$ and $\kappa_2$ are calculated in real-time based on the estimated wheel loads.

*3) Online Optimization*

The choice of optimization method depends on the problem at hand, the specific requirements, and the nature of the objective function and constraints. It is often beneficial to experiment with multiple methods and compare their performance to determine which approach is best suited for a particular optimization problem. In our case, a set of distinct optimization methods are implemented and compared from the point of view of efficiency and convergence speed including Active Set, Particle Swarm Optimization (PSO), and Sequential Quadratic Programming (SQP). The latter exhibited the most efficient performance to the problem at hand.

The general form of a nonlinearly constrained optimization problem can be given as (40).

$$\min_{x \in \mathcal{R}^n} f(x) \quad \text{subject to} \begin{cases} c_i(x) = 0 & \forall\, i \in \mathcal{E} \\ c_i(x) \geq 0 & \forall\, i \in \mathcal{I} \end{cases} \tag{40}$$

where f and $c_i$ are smooth scalar functions over $A \subset \mathcal{R}^n$, $\mathcal{E}$ denotes the set of equality constraints and $\mathcal{I}$ the set of inequality constraints. The SQP algorithm replaces the objective function with the quadratic approximation (41) and replaces the constraint functions with linear approximations.

$$q_k(d) = \nabla f(x_k)^T d + \frac{1}{2} d^T \nabla^2_{xx} \mathscr{L}(x_k, \lambda_k) d \tag{41}$$

**Algorithm 1** Online Two-Step Optimization

**Require:** $M_z$
  **if** $|M_z| \leq \underline{M_z}$ **then** ▷ $\underline{M_z}$: positive lower threshold for $M_z$
    $q \leftarrow n \leftarrow 0$
  **else if** $\underline{M_z} < |M_z| \leq \overline{M_z}$ **then**
    $q \leftarrow n \leftarrow 0.5$
  **else** ▷ $\overline{M_z}$: positive upper threshold for $M_z$
    $q \leftarrow n \leftarrow 1$
  **end if**
  $x = \arg\min_x \; f(T_{(x)},\, \omega,\, \eta_{\,(T,\,\omega)})$ ▷ x = [p, k]

where $\mathscr{L}$ is the Lagrangian and step d is calculated by solving the quadratic subprogram (42) (which is easier to solve and its objective function can reflect the nonlinearities of the original problem).

$$\begin{aligned} \min \{q_k(d) \;:\; & c_i(x_k) + \nabla c_i(x_k)^T d \leq 0,\; i \in \mathcal{I}; \\ & c_i(x_k) + \nabla c_i(x_k)^T d = 0,\; i \in \mathcal{E}\} \end{aligned} \tag{42}$$

The computation of $\nabla^2_{xx} \mathscr{L}(x_k, \lambda_k)$ is replaced by the BFGS (Broyden-Fletcher-Goldfarb-Shanno) approximation $B_k$, which is updated at each iteration, see [41]. The local convergence of the SQP approach is satisfied when $(x^*, \lambda^*)$ satisfies the second-order sufficiency conditions. If the starting point $x_0$ is sufficiently close to $x^*$, and the Lagrange multiplier estimates $\lambda_k$ remain sufficiently close to $\lambda^*$, then the sequence generated by setting $x_{k+1} = x_k + d$ converges to $x^*$ at a second-order rate, where $k$ is an iteration index.

The method is implemented by minimizing a cost function $f(x)$, representing a quantitative measure of the performance of the system under study. Since the constraints are already imposed at the low level and linearly carried by the parameters $p, k, q, n$, one can define the quadratic optimization problem as (43), where $x = [p\ k\ q\ n]^T$ represents the vector of the optimization variables. $l_b = [0\,0\,0\,0]^T$ and $u_b = [1\,1\,1\,1]^T$ are the lower and upper bounds for $x$ respectively. $x_0$ is initialized by assigning $0.5$ to each variable as a midway between $l_b$ and $u_b$.

$$\min_x f(x) \quad \text{subject to} \begin{cases} Ax \leq b \\ l_b \leq x \leq u_b \end{cases} \tag{43}$$

The cost function reflects the total power consumption of the motors (44). The driving/braking torques depend on $T_m, M_z$ and $p, k, q, n$. With reformulation, $f(x)$ is transformed into an equation governed by the high-level generated control inputs, and function of the optimization parameters.

$$f(x) = \sum_{i=1}^{4} \frac{T_i(x)\,\omega_i}{\eta_i^{sign(T_m)}} \quad \text{where } x = [p, k, q, n] \tag{44}$$

We observed that parameters $q$ and $n$ carried a singular value 1, reflecting the generation of $M_z$ through braking torques only. Its justification lies in the regenerative braking system (RBS), where the system favors the activation of DYC through braking to gain energy instantaneously. However, by braking repeatedly, the chassis loses its inertia and is forced to re-accelerate to compensate for the errors in $V_x$, consequently losing energy. Hence, the optimization problem was

**Algorithm 2** Offline Optimization Algorithm

**procedure** GET-Q,N($M_z$)
  **if** $|M_z| \leq \underline{M_z}$ **then**
    Activate DYC using traction torques only
  **else if** $\underline{M_z} < |M_z| \leq \overline{M_z}$ **then**
    Activate DYC using half traction/braking torques
  **else**
    Activate DYC using braking torques only
  **end if**
**end procedure**
**procedure** GET-P,K($M_z$, $T_m$, $q$, $n$, $\omega_i$, $\eta_i$)
  **if** $T_m \geq 0$ **then**
    **if** $\frac{\omega_1}{\eta_{k,1}^{sign(T_m)}} + \frac{\omega_2}{\eta_{k,2}^{sign(T_m)}} \geq \frac{\omega_3}{\eta_{k,3}^{sign(T_m)}} + \frac{\omega_4}{\eta_{k,4}^{sign(T_m)}}$ **then**
      Switch to the front-wheel traction driving mode
    **else**
      Switch to the rear-wheel traction driving mode
    **end if**
  **else**
    **if** $\frac{\omega_1}{\eta_{k,1}^{sign(T_m)}} + \frac{\omega_2}{\eta_{k,2}^{sign(T_m)}} \geq \frac{\omega_3}{\eta_{k,3}^{sign(T_m)}} + \frac{\omega_4}{\eta_{k,4}^{sign(T_m)}}$ **then**
      Switch to the rear-wheel traction driving mode
    **else**
      Switch to the front-wheel traction driving mode
    **end if**
  **end if**
  **if** $M_z \leq 0$ **then** ▷ $-rM_z/t_r \geq 0$
    **if** $\frac{-q\omega_1}{\eta_{k,1}^{sign(T_m)}} + \frac{(1-q)\omega_2}{\eta_{k,2}^{sign(T_m)}} \geq \frac{-n\omega_4}{\eta_{k,4}^{sign(T_m)}} + \frac{(1-n)\omega_3}{\eta_{k,3}^{sign(T_m)}}$ **then**
      Generate $M_z$ on the rear axle's axis of rotation
    **else**
      Generate $M_z$ on the front axle's axis of rotation
    **end if**
  **else**
    **if** $\frac{-q\omega_2}{\eta_{k,2}^{sign(T_m)}} + \frac{(1-q)\omega_1}{\eta_{k,1}^{sign(T_m)}} \geq \frac{-n\omega_3}{\eta_{k,3}^{sign(T_m)}} + \frac{(1-n)\omega_4}{\eta_{k,4}^{sign(T_m)}}$ **then**
      Generate $M_z$ on the rear axle's axis of rotation
    **else**
      Generate $M_z$ on the front axle's axis of rotation
    **end if**
  **end if**
**end procedure**

divided into two steps and denoted by two-step optimization given in algorithm 1. In the first step, $q, n$ (corresponding to traction/braking left/right allocation) are determined based on multi-objectives considering safety, comfort, and performance, while in the second step $p, k$ (for front/rear allocation) are determined by minimizing the cost function, considering the preassigned values for $q, n$. The parameters $q, n$ are adapted based on the magnitude of the yaw moment $M_z$. In normal driving conditions (low $|M_z|$), it prioritizes traction torques for a comfortable ride and higher speed. In mid-range $|M_z|$, it balances traction and braking torques to maintain stability and conserve energy. Finally, in critical scenarios (high $|M_z|$), it emphasizes braking torques for safety.

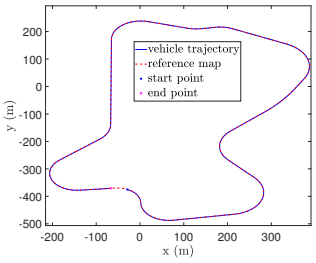


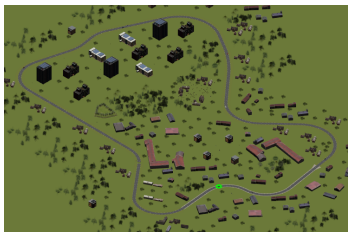

Fig. 12: Vehicle Trajectory - Sc1

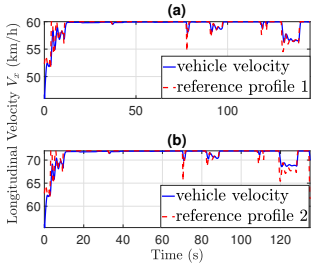


Fig. 13: Long. Velocity - Sc1

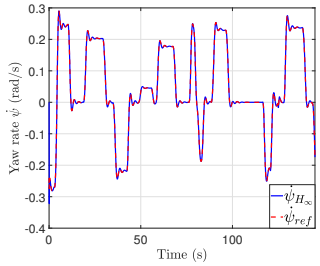


Fig. 14: Yaw Rate - Sc1

*4) Offline Optimization*

Ordinarily, strategies in the framework of offline optimization are executed based on data-driven constructed look-up tables or maps. In this work, the cost function (44) is analyzed offline as the dependent variables $T_m, M_z, \omega_i, \eta_i$ cover their ranges, and Algorithm 2 is devised based on the post-analysis. Algorithm 2 is implemented therefore to determine the parameters $p, k, q, n$ values in real-time.

## VI. Simulation Results

The proposed architectures are implemented and tested in a co-simulation between Simulink/MatLab and SCANeR™ Studio vehicle dynamics simulator. The controlled steering angle is fed via a steering system to the SCANeR vehicle considering a linear proportion between the steering wheel and the front wheels. In order to have a better insight into the behavior of each architecture, the following cost variables are introduced:

- Root Mean Square of the lateral error: $\sqrt{\frac{1}{t_{end}} \int_0^{t_{end}} e_y^2 \, dt}$
- Maximum lateral error: $e_{y,max}$
- Accumulated Energy Consumption: $E_m$ (see Fig. 9)
- Actuators usage (to assess the actuator performance):
  1) AFS: $\sqrt{\frac{1}{t_{end}} \int_0^{t_{end}} \delta_c^2 \, dt}$
  2) In-wheel motors: $\sqrt{\frac{1}{t_{end}} \int_0^{t_{end}} M_z^2 \, dt}$; $\sqrt{\frac{1}{t_{end}} \int_0^{t_{end}} T_m^2 \, dt}$

During the discussion, the cost variables considered may include the lateral error and the yaw moment. It is important to note that not all figures will incorporate all the cost variables. For each specific case scenario, we will introduce the relevant cost variables to demonstrate and highlight specific aspects. In addition, due to space constraints, some figures representing the low level are included for one approach only, allowing us to present both centralized and decentralized approaches.

A case study is performed considering two scenarios: An urban environment denoted by the "Urban Map" (Fig. 12) and

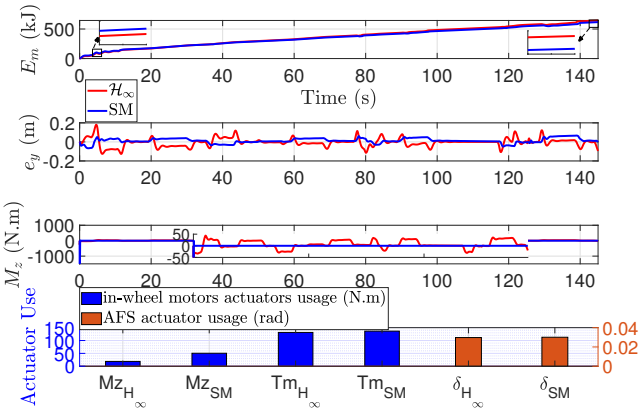


Fig. 15: SM and $\mathcal{H}_\infty$: cost variables - Low $V_x$ - Sc1 (a)

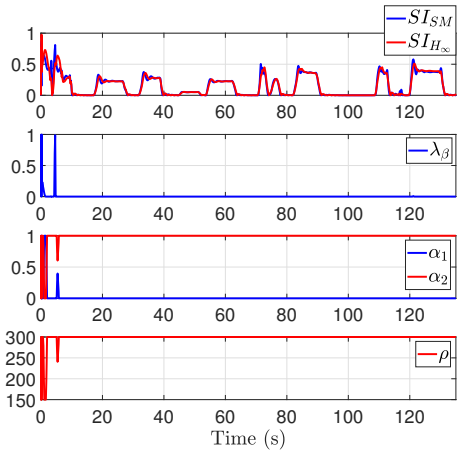


Fig. 16: Decision Parameters of SM and $\mathcal{H}_\infty$ - Sc1 (b)

a critical scenario given by the "Infinity Loop" (Fig. 25). The scenarios are elected with the aim of observing the performance and energy consumption of the architectures in a daily urban environment (Scenario 1) and the leading demeanor of the torque allocation strategies in hard road constraints (Scenario 2). Scenario 1 will focus on presenting the low level outcomes of the decentralized approach, while Scenario 2 will showcase the low level results of the centralized approach.

### A. *Scenario 1 (Sc1): Urban Map*

The first scenario is carried out on the track given in Fig. 12. The total distance from the start to the end point along the curved path is approximately 2.3 $km$.

The scenario is divided into two scenes depending on the reference velocity profile. The longitudinal velocity of the vehicle and the two reference profiles are given in Figures 13-(a) and 13-(b), where (a) corresponds to reference profile 1 (low velocity), and (b) refers to reference profile 2 (higher velocity than (a)). For the centralized $\mathcal{H}_\infty$ approach, the reference generated yaw rate $\dot{\psi}_{ref}$ (for the aim of path-tracking) is given in Fig. 14 with the vehicle yaw rate. This scenario will focus on the comparison of the proposed architectures at the high and low levels separately. It is known that STSM control has a chattering problem and reveals singularity in the

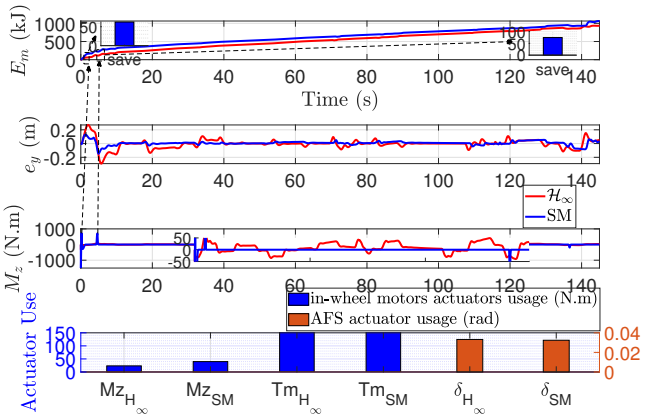


Fig. 17: SM and $\mathcal{H}_\infty$: cost variables - High $V_x$ - Sc1 (b)

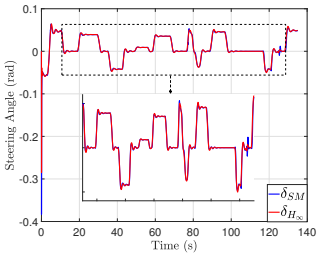


Fig. 18: Steering Angles - Sc1

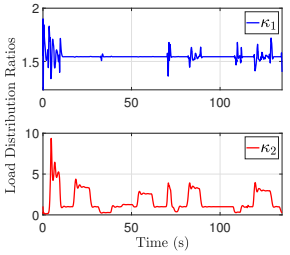


Fig. 19: $\kappa_1$ and $\kappa_2$ - Sc1 (b)

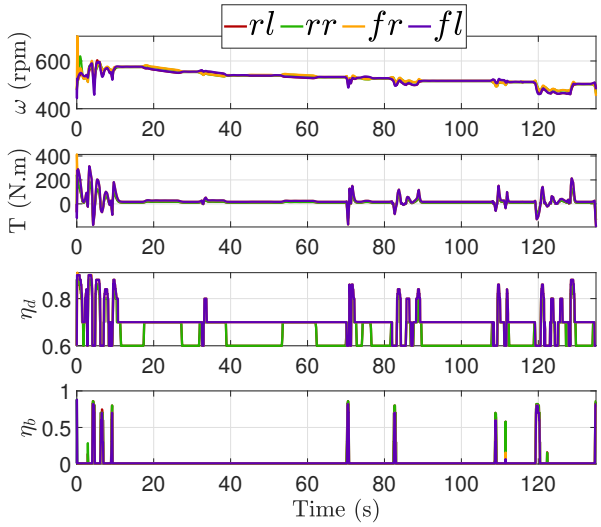


Fig. 20: Efficiency Estimation for Dynamic Strategy - Sc1 (b)

solution. On the other hand, $\mathcal{H}_\infty$ control is an optimal control that minimizes the energy-to-energy induced gain. Consequent to the aforementioned statements, energy consumption will be studied at the high level.

#### 1) *High-Level Comparison*

The implication behind the high-level comparison is the contrast in the generation of control inputs from various control techniques. The distinction between the two approaches is not confined to the performance, yet also to the consumed energy. The objective is to examine the influence of generating $\delta_c$ and $M_z$ by both centralized and decentralized approaches. Starting with Sc1-(a) corresponding to a low reference velocity

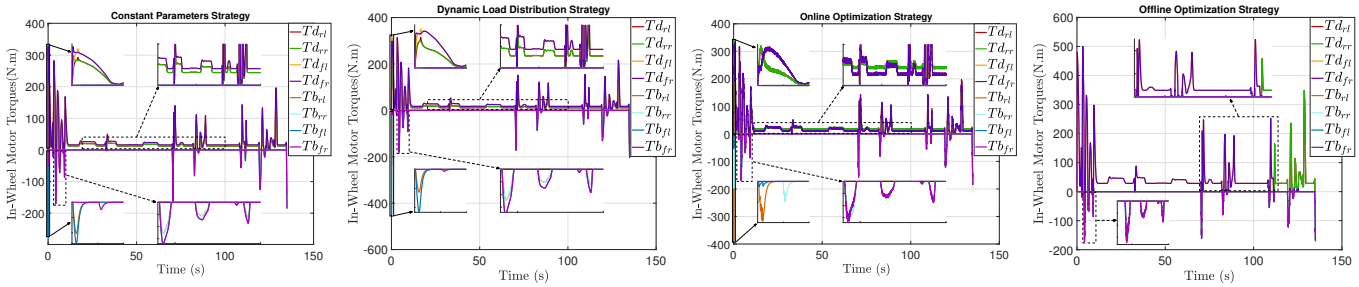


Fig. 21: In-Wheel Motors Driving and Braking Torques of the Proposed Strategies: Decentralized Approach - Sc1 (b)

profile, the cost variables of the two approaches are given in Fig. 15. The lateral error $e_y$ of the centralized approach exhibited higher overshoots than the decentralized one. At the beginning of the test, the vehicle accelerates to track the desired velocity. As a consequence, high $M_z$ is demanded by the Sliding Mode (SM) controller to retrieve the stability instantly. Subsequently, high energy consumption is noted for SM with peak usage of the actuators. $\mathcal{H}_\infty$ on the other hand gradually restored the stability by demanding lower $M_z$ and consequently lower energy consumption (Fig. 16 shows stability objective promotion). Hence, at about $6s$, the energy consumed by the vehicle using the SM controller revealed a higher value than the $\mathcal{H}_\infty$ controller. However, over the horizon, $M_z$ has been progressively generated by the centralized approach to aid the AFS with lateral control (since the centralized is a MIMO system). Therefore, at the end of the test, the energy consumed using $\mathcal{H}_\infty$ control is recorded higher than using SM control, although the in-wheel actuators usage of $\mathcal{H}_\infty$ control is lower than SM control. Alternatively, Sc1-(b) has shown that the energy consumption in critical situations of the vehicle using the SM controller is excessive enough to dominate the consumed energy using $\mathcal{H}_\infty$ control. Fig. 17 shows the yaw moment demand of the SM controller and the correspondent consumed energy.

Scenario 1 has shown that at low velocity, the accumulation of energy consumed by frequently demanding low amplitude of $M_z$ using $\mathcal{H}_\infty$ control, exceeds the energy consumption using the SM control. Conversely, at high velocities, the cumulation of energy through high amplitude demand of $M_z$ using SM control transcends the consumed energy using $\mathcal{H}_\infty$ control.

*2) Low-Level Comparison*

The generation of the control inputs at the high level is supervened by its realization at the actuators designated at the low level. From now on, Sc1-(b) is applied. The controlled steering angles of the SM and $\mathcal{H}_\infty$ approaches are given in Figure 18. Figure 19 shows the load distribution ratios of the dynamic load distribution allocation strategy based on the decentralized approach only due to the lack of space. $\kappa_1$ indicates that the rear/front load distribution is biased towards the front axle by roughly 1.5 times the rear axle, whereas $\kappa_2$ reveals a fluctuation in the left/right load distribution that attains 10 times the opposite side. The traction and braking torques of the four allocation strategies for the decentralized approach can be observed in Figure 21. The dynamic strategy revealed an obvious bias towards the front axle compared

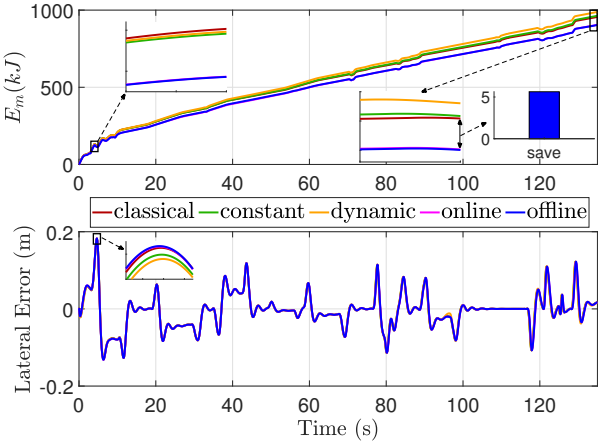


Fig. 22: Centralized Approach: cost variables - Sc1 (b)

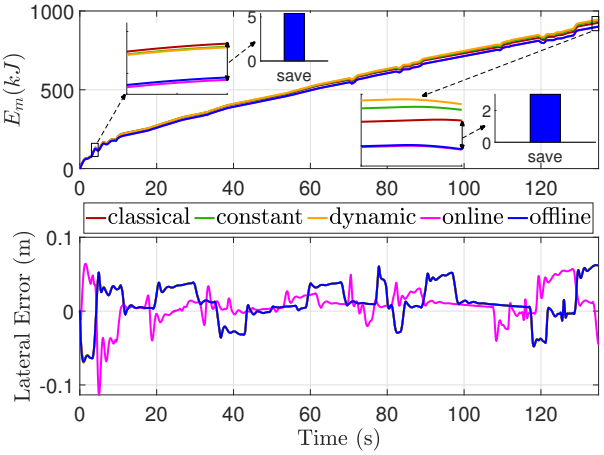


Fig. 23: Decentralized Approach: cost variables - Sc1 (b)

to the constant parameters strategy. The online optimization strategy exhibited filtered oscillations by virtue of the actuator model, while the offline optimization strategy exposed a non-oscillatory dispersed front-wheel or rear-wheel drive. The estimation of the driving and regenerative braking efficiencies $\eta_d$ and $\eta_b$ respectively is shown for the dynamic strategy (for the decentralized approach) only due to lack of space. Figure 20 displays the variation of $\eta_d$ and $\eta_b$ as a function of motor rotational speed ($\omega$) and its corresponding total traction/braking torque ($T$). When the demanded torque is traction, no regenerative braking is presented ($\eta_b$ is minimum)

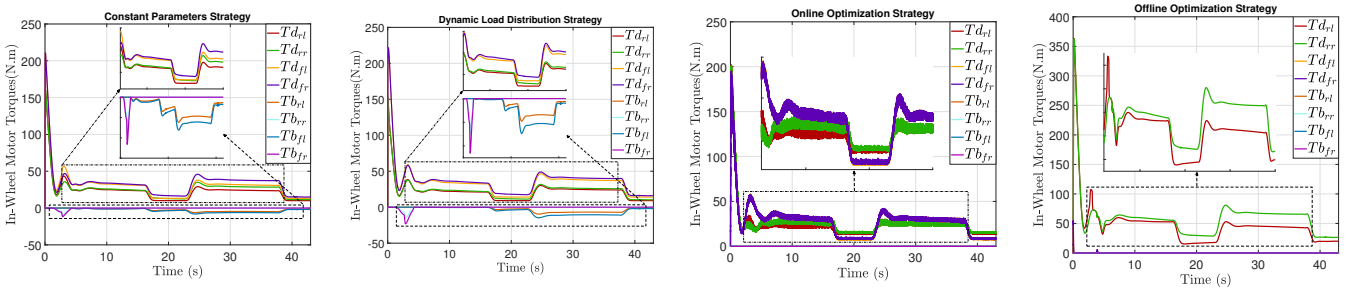


Fig. 24: In-Wheel Motors Driving and Braking Torques of the Proposed Strategies: Centralized Approach - Sc2 (b)

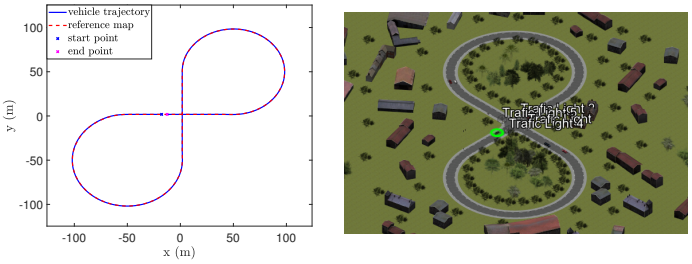


Fig. 25: Vehicle Trajectory - Sc2

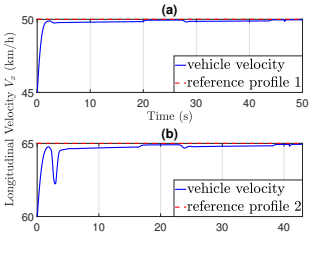


Fig. 26: Long. Velocity - Sc2

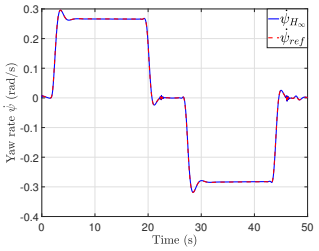


Fig. 27: Yaw Rate - Sc2 (a)

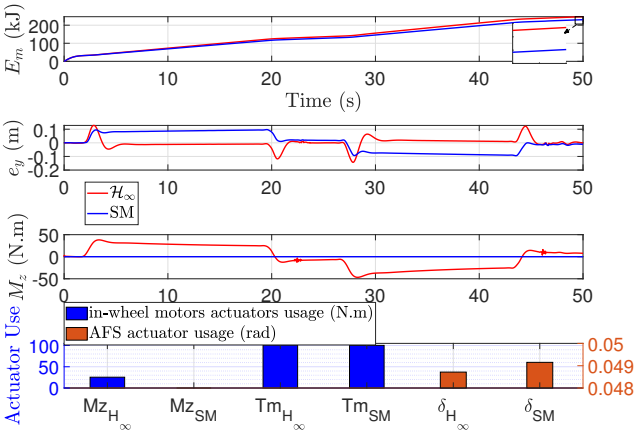


Fig. 28: SM and $\mathcal{H}_\infty$: cost variables - Sc2 (a)

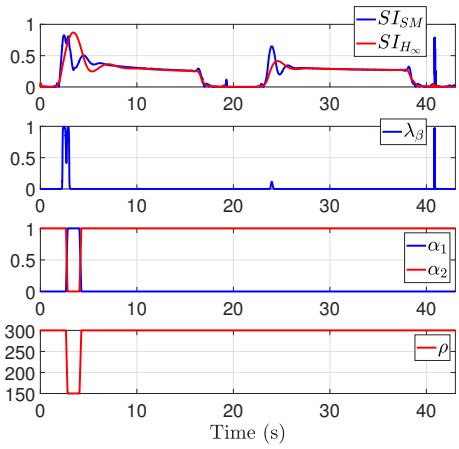


Fig. 29: Decision Parameters of SM and $\mathcal{H}_\infty$ - Sc2 (b)

and vice versa. Moreover, since the front axle motors generated torques higher than the rear axle motors, they have operated in higher efficiency zones.

The four allocation strategies are contrasted from the viewpoint of vehicle accumulated energy consumption and the lateral displacement error. Figure 22 reveals the cost variables of the four strategies based on the centralized approach. Two scenes will be discussed in this scenario: the beginning and end of the test. In the beginning, the high acceleration demanded by the vehicle resulted in distinct amounts of energy consumption for each allocation strategy, where the classical strategy marked the highest consumption followed by the dynamic and constant strategies. However, this observation is altered at the end of the test, where the highest energy consumption is recorded for the dynamic strategy, with an approximately similar consumption for the classical and constant parameters strategy. This reflects that the balanced load transfer (constant or dynamic) preserved the stability at the cost of energy consumption, at low velocities. With the salutary objective to minimize energy consumption through optimal allocation, the online and offline optimization strategies have revealed a considerable reduction in energy consumption along the whole trajectory. The amount of percentage energy saved has reached $5.6\%$ w.r.t the classical vehicle at the end of the test. The four strategies are compared likewise for the decentralized approach and given in Figure 23. Similar to the centralized approach, the allocation strategies based on the decentralized approach have exposed an analogous behavior yet with disparate amounts of energy consumption.

This test has demonstrated the major energy economy of online and offline optimization strategies based on both centralized and decentralized approaches in daily urban environments. Further, it has manifested that the constant and dynamic strategies turn out to be energy quasi-optimal during non-ordinary driving situations (high velocity and consequently

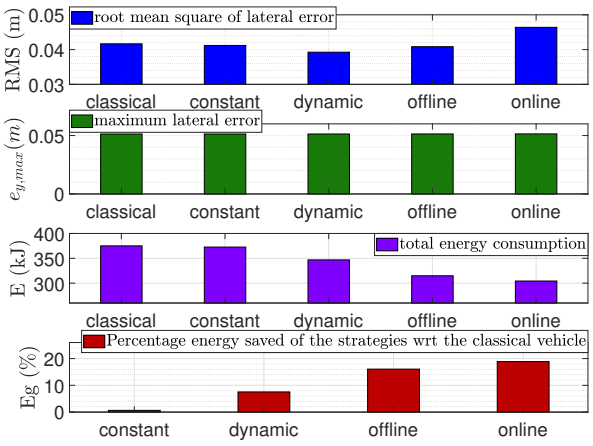


Fig. 30: Decentralized Approach: cost variables - Sc2 (b)

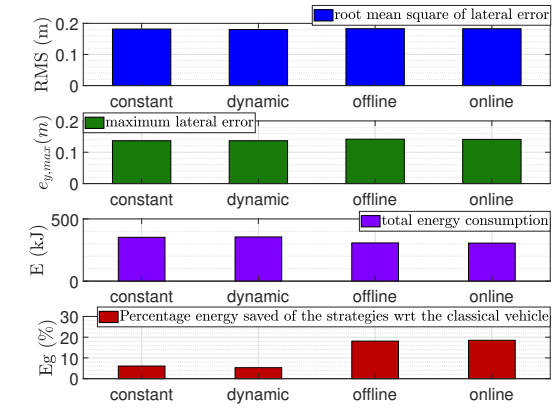


Fig. 31: Centralized Approach: cost variables - Sc2 (b)

higher lateral acceleration). Therefore, a second scenario will be performed to distinguish the influence of the proposed strategies during critical situations.

### *B. Scenario 2 (Sc2): Infinity Loop*

The second scenario is executed on the hard road geometry track presented in Fig. 25. The total curvilinear length of the road is $672\ m$ in this case. Similar to Scenario 1, two tests are performed in the second Scenario depending on the reference velocity profiles given in Fig. 26-(a) and (b). Starting with Sc2-(a) presenting a low-velocity profile, the reference yaw rate generated by the centralized approach for the trajectory following is given in Fig. 27. Both the decentralized and centralized approaches are compared at the high level based on the classical allocation strategy. Figure 28 shows the cost variables of both approaches. Similar to Sc1-(a) for low reference velocity, Sc2-(a) revealed that the vehicle based on the SM controller has recorded lower energy consumption than using $\mathcal{H}_\infty$ control for the same reasons discussed in Sc1. The lateral errors of the SM controller exhibited a positive constant steady-state error on the high curvature portions, while it converged to zero with higher overshoots in the $\mathcal{H}_\infty$ control case. The total energy consumed was higher in the $\mathcal{H}_\infty$ controlled vehicle due to the frequent generation of $M_z$ to assist AFS with lateral control. Contrary to the SM case, where no occurrence of $M_z$ generation was observed due to the absence of instability risk. As for the high-velocity profile executed in Sc2-(b), the decision parameter $\lambda_\beta$ and the weighting parameter $\rho$ of the decentralized and the centralized approaches respectively are given as a function of the stability index in Fig. 29. It can be noticed that the stability objective is promoted more frequently in the decentralized approach than in the centralized one ($\lambda_\beta$ varied more than $\rho$). The traction and braking torques of the four proposed allocation strategies based on the centralized approach are given in Fig. 24. The torques exhibited similar behavior as in Sc1 however more dispersed in the centralized approach due to the generation of $M_z$. The four allocation strategies are compared for both the decentralized and the centralized approaches based on the defined cost variables. Hereafter, the classical allocation strategy based on the SM control will be the "reference vehicle" to contrast the remnant strategies. Figure 30 shows the cost variables based on the decentralized approach. The root mean square (RMS) of the lateral error is studied in each strategy. The online optimization strategy revealed the highest RMS with the lowest value recorded to the dynamic strategy. Similarly, for the maximum lateral error, the dynamic strategy exhibited the lowest value. As for the total amount of accumulated energy consumption, the classical strategy has manifested to be the highest. Compared to the reference vehicle, the amount of energy saved by the constant, dynamic, offline, and online strategies are respectively $0.6\%$, $7.5\%$, $16.1\%$, and $18.9\%$. Similarly, Figure 31 presents the cost variables based on the centralized approach. The RMS and the maximum lateral error of the four strategies are roughly identical. However, the amount of total energy consumption has varied. Contrasted with the reference vehicle, the constant strategy has now saved $6\%$, while the dynamic, offline, and online strategies have saved respectively $5.3\%$, $18.1\%$, $18.8\%$. This scenario has demonstrated the supreme energy economy of the online and offline optimization strategies compared to a simple allocation strategy for in-wheel-driven vehicles. It has been shown that the proposed strategies are most effective during critical driving situations for instance high curvatures, acceleration, braking, and stability retaining. The dynamic strategy exhibited the most stable behavior with an energy economy, manifesting that an optimal torque allocation based on a dynamically balanced distribution of the loads between the front/rear and left/right sides results in an energy economy.

### *C. Recap*

The executed scenarios have demonstrated the major influence of each allocation strategy based on the two approaches (centralized and decentralized). Scenario 1 manifested the capability of reducing energy consumption in a daily urban environment by implementing online or offline optimization strategies. It also showed that the remnant strategies are energy quasi-optimal during non-ordinary situations. The second scenario demonstrated the significant energy saving for both approaches using the offline and online optimization allocation strategies; and manifested the major effect of static and

TABLE I: Summary for the comparison of the control architectures

| Control Architectures | Decentralized STSM | | | | Centralized LPV/$\mathcal{H}_\infty$ | | | |
|---|---|---|---|---|---|---|---|---|
| | constant | dynamic | offline | online | constant | dynamic | offline | online |
| Energy Gain (%) - sc1 | 0 | 0 | 3 | 3.1 | 0 | 0 | 5.6 | 5.7 |
| Energy Gain (%) - sc2 | 0.6 | 7.5 | 16.1 | 18.9 | 6 | 5.3 | 18.1 | 18.8 |
| Computational Time | fast | fast | fast | slow | fast | fast | fast | relatively slow |
| $TWU$-based Stability Performance | highly stable | most stable | stable | stable | highly stable | most stable | stable | stable |

dynamic load distribution strategies for the energy economy in critical driving situations. A summary of the architectures' performance is given in Table I. The online optimization approach unveiled the utmost substantial energy savings, but the offline optimization strategy is much faster and can be more suitable for real-time implementation using basic hardware. As for the constant and dynamic strategies, they revealed the highest stability and comfort performance. Indeed, the vehicle maintains stability across all allocation strategies, since as long as $p, k, q, n \in [0, 1]$ then $M_z$ is achieved. Nonetheless, thanks to the balanced load distribution especially with the dynamic strategy that optimally allocates torque to each wheel within its friction circle, it significantly enhances vehicle stability, particularly in high-cornering maneuvers. So in conclusion, the online and offline strategies are stable and energy-optimal in all scenarios, while the dynamic and constant strategies are highly stable in all situations, and energy economic only in critical situations.

The scenarios demonstrated that $\mathcal{H}_\infty$ control proves to be a more cost-effective choice for the vehicle in high-velocity conditions, albeit it entails higher complexity. On the other hand, SM control offers economic advantages for the vehicle in low-velocity situations, while maintaining a simpler design. From Table I, the variation in the energy consumption values between the centralized and decentralized approaches can be noticed for the same low-level approach, especially for the constant strategy. The main objective is not to disclose specific values, as it can depend on the road situations, but rather to demonstrate that energy consumption must be assessed globally on the high and low levels.

A playlist of videos for the validation of the architectures can be seen at the following link: Validation Videos.

## VII. Conclusion

In this paper, two complete control architectures were developed based on centralized and decentralized approaches for lateral, longitudinal, and stability control. The STSM control technique is utilized for the decentralized approach, whereas the centralized approach is established by applying optimal $\mathcal{H}_\infty$ control. The generated high-level control inputs, $T_m$ and $M_z$, are realized using a novel torque distribution configuration at the low level according to the four parameters $p, k, q, n$. Then, four multi-objective allocation strategies were developed and compared for each high level approach. Finally, several testing scenarios are conducted to elucidate the leading influence of each control architecture in distinct driving situations. This paper highlights the imperative to globally assess energy consumption across the entire architecture, encompassing both high and low levels. A perspective work is to implement the proposed architectures on a real experimental vehicle on a testing platform and to extend the scope of energy consumption optimization from an instantaneous to a time horizon-based approach.

## Acknowledgments

This work is carried out within the framework of the V3EA project "Electric, Energy Efficient and Autonomous Vehicle" (2021-2025), funded by the Research National Agency (ANR) of the French government.

## Appendix

$$
\begin{aligned}
&a_{11} = -\mu\frac{l_f^2 C_f + l_r^2 C_r}{I_z V_x};\quad a_{12} = \mu\frac{l_r C_r - l_f C_f}{I_z}\\
&a_{21} = -1 + \mu\frac{l_r C_r - l_f C_f}{M V_x^2};\quad a_{22} = -\mu\frac{C_r + C_f}{M V_x}\\
&b_{11} = \mu\frac{l_f C_f}{I_z};\quad b_{12} = \frac{1}{I_z};\quad b_{21} = \mu\frac{C_f}{M V_x};\quad b_{22} = 0\\
&c_1 = \frac{1}{I_z};\quad c_2 = \frac{1}{M V_x}
\end{aligned}
\tag{45}
$$

## References

[1] W. Wang, T. Ma, C. Yang, Y. Zhang, Y. Li, and T. Qie, "A path following lateral control scheme for four-wheel independent drive autonomous vehicle using sliding mode prediction control," *IEEE Transactions on Transportation Electrification*, vol. 8, no. 3, pp. 3192–3207, 2022.

[2] A. Chokor, R. Talj, M. Doumiati, A. Hamdan, and A. Charara, "A comparison between a centralized multilayer lpv/h$_\infty$ and a decentralized multilayer sliding mode control architectures for vehicle's global chassis control," *International Journal of Control*, vol. 95, pp. 1–32, 07 2020.

[3] X. Cao, T. Xu, Y. Tian, and X. Ji, "Gain-scheduling lpv synthesis $h_\infty$ robust lateral motion control for path following of autonomous vehicle via coordination of steering and braking," *Vehicle System Dynamics*, vol. 61, no. 4, pp. 968–991, 2022.

[4] A. Chokor, M. Doumiati, R. Talj, and A. Charara, "Design of a new gain-scheduled lpv/ controller for vehicle's global chassis control," in *2019 IEEE 58th Conference on Decision and Control (CDC)*, 2019, pp. 7602–7608.

[5] W. Botes, T. R. Botha, and P. S. Els, "Real-time lateral stability and steering characteristic control using non-linear model predictive control," *Vehicle System Dynamics*, vol. 61, no. 4, pp. 1063–1085, 2022.

[6] M. Waqas and P. Ioannou, "Automatic vehicle following under safety, comfort, and road geometry constraints," *IEEE Transactions on Intelligent Vehicles*, vol. 8, no. 1, pp. 531–546, 2023.

[7] X. Zhou, Z. Wang, H. Shen, and J. Wang, "Robust adaptive path-tracking control of autonomous ground vehicles with considerations of steering system backlash," *IEEE Transactions on Intelligent Vehicles*, vol. 7, no. 2, pp. 315–325, 2022.

[8] G. Chen, J. Yao, H. Hu, Z. Gao, L. He, and X. Zheng, "Design and experimental evaluation of an efficient mpc-based lateral motion controller considering path preview for autonomous vehicles," *Control Engineering Practice*, vol. 123, p. 105164, 2022.

[9] H. Peng, W. Wang, Q. An, C. Xiang, and L. Li, "Path tracking and direct yaw moment coordinated control based on robust mpc with the finite time horizon for autonomous independent-drive vehicles," *IEEE Transactions on Vehicular Technology*, vol. 69, no. 6, pp. 6053–6066, 2020.

[10] Y. Zou, N. Guo, and X. Zhang, "An integrated path-following and yaw motion control strategy for autonomous distributed drive electric vehicles with differential steering," in *2019 IEEE Intelligent Vehicles Symposium (IV)*, 2019, pp. 1987–1992.

[11] A. Chebly, R. Talj, and A. Charara, "Coupled longitudinal/lateral controllers for autonomous vehicles navigation, with experimental validation," *Control Engineering Practice*, vol. 88, pp. 79–96, 2019.

[12] Y. M. Mok, L. Zhai, C. Wang, X. Zhang, and Y. Hou, "A post impact stability control for four hub-motor independent-drive electric vehicles," *IEEE Transactions on Vehicular Technology*, vol. 71, no. 2, pp. 1384–1396, 2022.

[13] C. Liu, H. Liu, L. Han, W. Wang, and C. Guo, "Multi-level coordinated yaw stability control based on sliding mode predictive control for distributed drive electric vehicles under extreme conditions," *IEEE Transactions on Vehicular Technology*, vol. 72, no. 1, pp. 280–296, 2023.

[14] N. Ahmadian, A. Khosravi, and P. Sarhadi, "Driver assistant yaw stability control via integration of afs and dyc," *Vehicle System Dynamics*, vol. 60, no. 5, pp. 1742–1762, 2022.

[15] X. Li, N. Xu, K. Guo, and Y. Huang, "An adaptive smc controller for evs with four iwms handling and stability enhancement based on a stability index," *Vehicle System Dynamics*, vol. 59, no. 10, pp. 1509–1532, 2021.

[16] G. Park and S. B. Choi, "A model predictive control for path tracking of electronic-four-wheel drive vehicles," *IEEE Transactions on Vehicular Technology*, vol. 70, no. 11, pp. 11 352–11 364, 2021.

[17] W. Wang, Y. Zhang, C. Yang, T. Qie, and M. Ma, "Adaptive model predictive control-based path following control for four-wheel independent drive automated vehicles," *IEEE Transactions on Intelligent Transportation Systems*, vol. 23, no. 9, pp. 14 399–14 412, 2022.

[18] H. Jing, F. Jia, and Z. Liu, "Multi-objective optimal control allocation for an over-actuated electric vehicle," *IEEE Access*, vol. 6, pp. 4824–4833, 2018.

[19] J. Wang, S. Gao, K. Wang, Y. Wang, and Q. Wang, "Wheel torque distribution optimization of four-wheel independent-drive electric vehicle for energy efficient driving," *Control Engineering Practice*, vol. 110, p. 104779, 2021.

[20] X. Zhang, D. Göhlich, and J. Li, "Energy-efficient toque allocation design of traction and regenerative braking for distributed drive electric vehicles," *IEEE Transactions on Vehicular Technology*, vol. 67, no. 1, pp. 285–295, 2018.

[21] C. Jing, H. Shu, R. Shu, and Y. Song, "Integrated control of electric vehicles based on active front steering and model predictive control," *Control Engineering Practice*, vol. 121, p. 105066, 2022.

[22] A. K. Madhusudhanan and M. Corno, "Effect of a nu vinci type cvt based energy efficient cruise control on an electric vehicle's energy consumption," in *2022 European Control Conference (ECC)*, 2022, pp. 1722–1727.

[23] J. V. Alcantar and F. Assadian, "Vehicle dynamics control of an electric-all-wheel-drive hybrid electric vehicle using tyre force optimisation and allocation," *Vehicle System Dynamics*, vol. 57, no. 12, pp. 1897–1923, 2019.

[24] J. Torinsson, M. Jonasson, D. Yang, and B. Jacobson, "Energy reduction by power loss minimisation through wheel torque allocation in electric vehicles: a simulation-based approach," *Vehicle System Dynamics*, vol. 60, no. 5, pp. 1488–1511, 2022.

[25] A. Mihály, P. Gáspár, and H. Basargan, "Maximizing autonomous in-wheel electric vehicle battery state of charge with optimal control allocation," in *2019 18th European Control Conference (ECC)*, 2019, pp. 250–255.

[26] C. Lin, S. Liang, J. Chen, and X. Gao, "A multi-objective optimal torque distribution strategy for four in-wheel-motor drive electric vehicles," *IEEE Access*, vol. 7, pp. 64 627–64 640, 2019.

[27] Z. Wang, C. Qu, L. Zhang, X. Xue, and J. Wu, "Optimal component sizing of a four-wheel independently-actuated electric vehicle with a real-time torque distribution strategy," *IEEE Access*, vol. 6, pp. 49 523–49 536, 2018.

[28] H. Laghmara, "Yaw moment lyapunov based control for in-wheel-motor-drive electric vehicle," vol. 50, 07 2017.

[29] W. Chen, H. Xiao, Q. Wang, L. Zhao, and M. Zhu, *Integrated vehicle dynamics and control*, 04 2016.

[30] *SCANeR - AVSimulation*, SCANeR Studio Simulator. [Online]. Available: https://www.avsimulation.com/scaner/

[31] V. Utkin, "On convergence time and disturbance rejection of super-twisting control," *IEEE Transactions on Automatic Control*, vol. 58, no. 8, pp. 2013–2017, 2013.

[32] F. Tarhini, R. Talj, and M. Doumiati, "Adaptive look-ahead distance based on an intelligent fuzzy decision for an autonomous vehicle," in *2023 IEEE Intelligent Vehicles Symposium (IV)*, 2023, pp. 1–8.

[33] R. Rajamani, *Vehicle Dynamics and Control*, 2nd ed. Springer, 2012.

[34] H.-S. Tan and J. Huang, "Design of a high-performance automatic steering controller for bus revenue service based on how drivers steer," *IEEE Transactions on Robotics*, vol. 30, no. 5, pp. 1137–1147, 2014.

[35] M. Doumiati, O. Sename, L. Dugard, J.-J. Martinez-Molina, P. Gaspar, and Z. Szabo, "Integrated vehicle dynamics control via coordination of active front steering and rear braking," *European Journal of Control*, vol. 19, no. 2, pp. 121–143, 2013.

[36] H. Atoui, O. Sename, V. Milanés, and J. J. Martinez, "Lpv-based autonomous vehicle lateral controllers: A comparative analysis," *IEEE Transactions on Intelligent Transportation Systems*, vol. 23, no. 8, pp. 13 570–13 581, 2022.

[37] P. Apkarian, P. Gahinet, and G. Becker, "Self-scheduled $\mathcal{H}_\infty$ control of linear parameter-varying systems: a design example," *Automatica*, vol. 31, no. 9, pp. 1251–1261, 1995.

[38] *Protean Electric PD18 In-wheel Electric Motor Datasheet*, Protean Electric. [Online]. Available: https://www.proteanelectric.com/f/2018/05/Pd18-Datasheet-Master.pdf

[39] N. Guo, X. Zhang, Y. Zou, B. Lenzo, G. Du, and T. Zhang, "A supervisory control strategy of distributed drive electric vehicles for coordinating handling, lateral stability, and energy efficiency," *IEEE Transactions on Transportation Electrification*, vol. 7, no. 4, pp. 2488–2504, 2021.

[40] L. Guo, X. Lin, P. Ge, Y. Qiao, L. Xu, and J. Li, "Torque distribution for electric vehicle with four in-wheel motors by considering energy optimization and dynamics performance," in *2017 IEEE Intelligent Vehicles Symposium (IV)*, 2017, pp. 1619–1624.

[41] F. E. Curtis, T. Mitchell, and M. L. Overton, "A bfgs-sqp method for nonsmooth, nonconvex, constrained optimization and its evaluation using relative minimization profiles," *Optimization Methods and Software*, vol. 32, no. 1, pp. 148–181, 2017.